Turkish Journal of Electrical Engineering & Computer Sciences

http://journals.tubitak.gov.tr/elektrik/

Research Article

Turk J Elec Eng & Comp Sci
(2023) 31: 53 – 76

doi:10.55730/1300-0632.3971

An effective Hilbert–Huang transform-based approach for dynamic eccentricity fault diagnosis in double-rotor double-sided stator structure axial flux permanent magnet generator under various load and speed conditions

Makan TORABI, Yousef ALINEJAD-BEROMI*
Department of Electrical Engineering, Semnan University, Semnan, Iran

Received: 04.09.2022 • **Accepted/Published Online:** 17.12.2022 • **Final Version:** 19.01.2023

Abstract: Eccentricity fault in double-sided axial flux permanent magnet generator is very difficult to be detected as the fault generated variations in terminal electrical parameters are very weak and chaotic, especially at the initial stages of the fault occurrence. In addition, one of the most important problems in any fault diagnosis approach is the investigation of load and speed variation on the proposed indices. To overcome the aforementioned difficulty and problems, this paper adopts a novelty detection algorithm based on Hilbert–Huang transform (HHT) which is a time-frequency signal analysis approach based on empirical mode decomposition and the Hilbert transform. It is well suited for reliable fault diagnosis since it is unaffected by transient conditions which make the diagnosis process incur into false alarms. The HHT-based methods has been demonstrated in recent years for rotor and bearing faults detection of induction machine and also for stator faults identification in PM synchronous machines with radial flux structure. This study explores the possibility of applying the technique to the detection of dynamic eccentricity faults in double-rotor double-sided stator structure axial flux permanent magnet generator under variable load and speed conditions. This approach relies on two steps: estimating the intrinsic mode functions (IMFs) by the empirical mode decomposition (EMD) and computing the instantaneous amplitude (IA) and instantaneous frequency (IF) of IMFs using the Hilbert transform. The more significant IMFs are determined by means of Hilbert spectrum, which is applied for accurate eccentricity fault diagnosis. The eccentricity severity can be evaluated based on the IMFs energy value. The theoretical basis of the proposed method is presented. The effectiveness of the proposed method is verified by a series of simulation and experimental tests under different conditions. The results show that the presented approach in this paper is robust against load and speed variations.

Key words: Double-sided axial flux permanent magnet generator, dynamic eccentricity fault diagnosis, stator currents, intrinsic mode function, empirical mode decomposition, Hilbert–Huang transform

1. Introduction

Permanent magnet (PM) machines have been extensively used in a variety of industrial applications and renewable energy generation due to their high power density, high efficiency, and simple controllability [1–5]. Among different types of PM machines, double structural axial flux PM machine (AFPM) is applied for direct driving of small scale-low speed turbines with wide speed variation because of its suitable performance [6–8]. In practice, AFPMs are subjected to various mechanical and electrical faults occurrence. Mechanical faults could be due to eccentricities, damaged rotor permanent magnets, misalignment, and asymmetries. One

*Correspondence: yalinejad@semnan.ac.ir

of the most common faults in AFPMs is static/dynamic eccentricity. In the dynamic eccentricity the rotor symmetrical axis is shifted with respect to the rotor rotation axis, which coincides with the stator symmetrical axis and a rotating minimum air gap will be created. The consequence of this fault is the nonuniformity of flux distribution between the rotor and stator poles which causes nonuniform magnetic poles formation and lead to entail vibration, acoustic noise, and ball bearing failure [9]. If the machine operation continues under dynamic eccentricity condition, the unbalanced magnetic force between rotor and stator will cause fault expansion intensification, rotor and stator abrasion, and eventually, machine breakdown. Thus, it is important to diagnose the dynamic eccentricity fault in initial stages of fault occurrence in order to avoid machine failure. Several methods have been developed for fault diagnosis in permanent magnet machines. These methods can be divided into five main categories: 1) magnetic flux analysis, 2) noise or vibration analysis, 3) torque profile analysis, 4) analytical methods based on machine modeling parameters estimation, and 5) analysis of the machine's current. The capabilities of each method for online or offline diagnosis under stationary or nonstationary conditions are different. Magnetic flux analysis is an accurate method for various fault diagnosis. In [10], no-load radial magnetic field and no-load Back-EMF are analysed for eccentric position diagnosis in external rotor permanent magnet synchronous motor and in [11] an online method for eccentricity fault diagnosis in axial flux machines based on indirect flux measurements is presented. The magnetic flux signal can be driven from the induced voltage of mounted search coils [12] and Hall Effect sensor [13, 14]. The magnetic field analysis method is appropriate for online diagnosis under nonstationary conditions, but the high cost and difficulty of mounting the search coils and sensors are the main drawbacks of this method. In [15] and [16], the analysis of acoustic noise is employed to introduce an index for online eccentricity and partial demagnetization detection. The main limitation of vibration and acoustic analysis method is the necessity of physical access to the machine and perpetual installation of sensors, which increases the system cost and reduces system reliability. In addition, various conditions may generate similar patterns in the vibration and acoustic noise, which leads to wrong judgement. In [17], spectrum analysis of the machine current and torque is applied to online rotor-bar faults diagnosis. Direct measurement of torque requires expensive sensors and is an invasive method. Therefore, the electromagnetic torque can be computed by considering the saturation through accurate analytical equations [18]. In [19], a knowledge graph method based on accurate modelling of direct-drive permanent magnet synchronous motor is proposed for the detection and location of the fault coil and in [20], the alteration in equivalent inductance has been applied to distinguish between eccentricity and partial demagnetization. Modelling and parameter estimation methods are sensitive, reliable, and more suitable for off-line diagnosis or nonstationary machine conditions.

The machine current signature analysis (MCSA) is the most common method for fault identification. The main advantage of MCSA method is that no expensive sensors are needed, and the applied procedures are not invasive and intricate [21, 22]. In this approach, frequency analysis using fast Fourier transform (FFT) is applied for fault diagnosis under stationary conditions [23]. The extended version of MCSA (transient MCSA) is applied for fault diagnosis under nonstationary conditions. In TMCAS procedure, time-frequency analysis methods are employed for feature extraction to diagnose fault [24]. Different time-frequency analysis techniques have been recommended to apply TMCSA. Short time Fourier transform (STFT) has been proposed as the developed version of Fourier transform for nonstationary signals [25, 26]. In STFT method, the obtained signal is divided into several time periods using windows with predetermined length and type and any section is analysed by Fourier transform. The main drawback of this technique is that the type and length of the window must be selected suitably depending on the intended application and frequency components, which are not a

theoretical process [26]. In order to analyse the signals with fast dynamics, multiresolution signal processing methods including wavelet transform have been applied [27]. In fact, wavelet transform makes it possible to vary the time and frequency resolution on time-frequency plane [28, 29]. The main drawback of this method is that once the wavelet function is chosen, it should be applied to analyse all the sampled data. Moreover, in a discrete wavelet with permanent sampling, frequency bands of scales are dependent on sampling frequency.

Recently, Hilbert-Huang transform (HHT) as a novel approach has been investigated for machine fault diagnosis under nonstationary condition. In [30] and [31], the HHT has been applied for broken rotor bars and bearing faults detection in an induction machine. The use of HHT for stator faults identification in PM synchronous machine with radial flux structure has been provided in [32] and [33].

Load and speed variation, along with eccentricity fault, directly affects the dynamic behaviours of eccentricity signatures that appear in the current spectrum of the generator. Such a problem is one of the most important problems in any fault diagnosis approach.

In this paper, a novelty detection algorithm based on Hilbert–Huang transform is provided to overcome the aforementioned problems for accurate dynamic eccentricity diagnosis in a double structural AFPM generator. In order to evaluate the validity of the proposed method, simulation and experiments for unsteady speed in the presence of linear and nonlinear load under healthy and different eccentricity severity conditions of generator have been performed.

This paper is organized as follows. Section 2 presents the theoretical analysis of dynamic eccentricity in double structural axial flux PM generator. In Section 3, the HHT and its application for dynamic eccentricity diagnosis under nonstationary condition are introduced. The simulation and experimental validation results that prove the effectiveness of the proposed method are elaborated in Section 4. Finally, Section 5 concludes the paper.

2. Theoretical analysis of dynamic eccentricity in the AFPM generator

Double-sided topology of AFPM generator in 3D plane is shown in Figure 1a, which is simulated in MAXWELL FEM software. The test generator used in this research consists of two rotor discs with surface-mounted permanent magnets and a double side stator with series-connected four coils per phase. The back EMF is generated in the coils due to the rotation of the rotor magnets. The coils have been located in the stator slots in such a way that the direction of air gap flux density is mainly axial, as shown in Figure 1b [34].

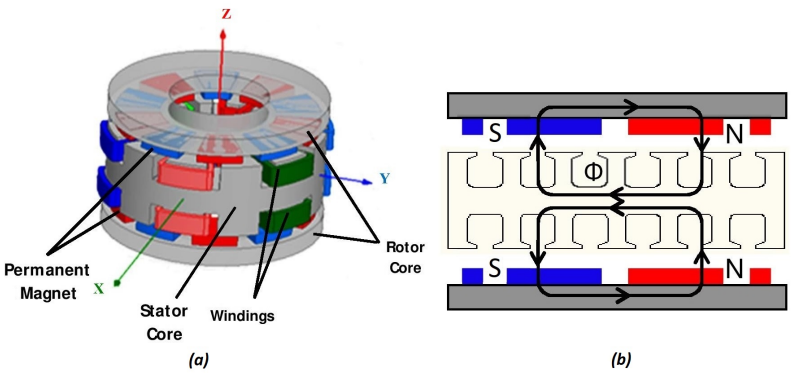

Figure 1. AFPM generator: (a) double-sided topology in 3D plane, (b) flux directions.

2.1. Dynamic eccentricity description

The eccentricity is a nonuniform air gap condition between the stator and the rotor, causing an asymmetric air gap flux distribution, which creates an unbalanced magnetic pull. This leads to vibrations, noise, and possibly destroying the bearings. If the machine operation continues under eccentricity condition, the unbalanced magnetic force may further increase and cause the rotor and stator to rub. Eccentricity faults can be categorized into three main types: static eccentricity (SE) (caused by an incorrect rotor and stator aligning during the machine assembly or due to the different mechanical and electrical stresses acting on the machine [35]); dynamic eccentricity (DE) (caused by a bend in the machine shaft, bearing wear, mechanical and thermal stresses acting on the shaft [36]); and mixed eccentricity (ME) (combination of both static and dynamic eccentricities).

As shown in Figure 2a, the air gap length g_0 is symmetrical along the circumferential direction under healthy condition. The rotor position with respect to the stator under static eccentricity in 2D plane is shown in Figure 2b. In the static eccentricity, the symmetrical axis of the rotor coincides with its rotating axis but is dislocated from the stator symmetrical axes. In this case, the axis of the rotor deviates from the axis of the stator by an angle which causes a nonuniform air gap but the position of the minimum air gap length is fixed in space.

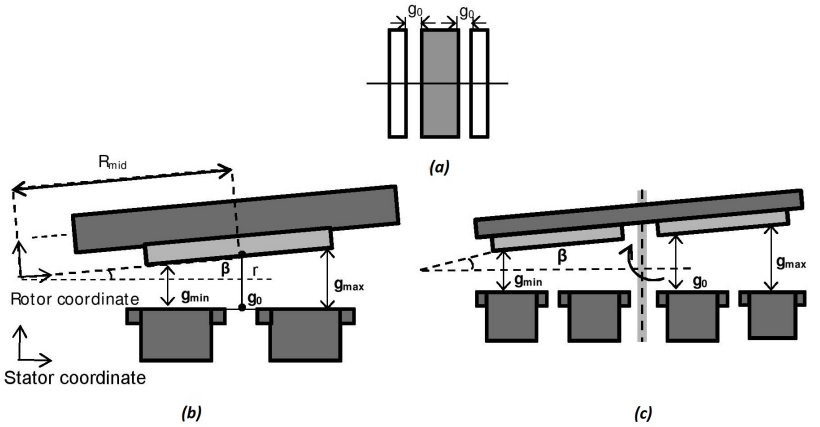

Figure 2. Double-sided topology of AFPM machine in 2D plane: (a) healthy condition, (b) static eccentricity condition, (c) dynamic eccentricity condition.

The static eccentricity factor (SEF) is defined as:

$$SEF = \frac{r}{g_0} \times 100\% \tag{1}$$

where g_0 is the air gap length in the normal operation of the machine and r is calculated as:

$$r = R_{\text{mid}} \times \sin(\beta) \tag{2}$$

$$R_{\text{mid}} = \frac{R_{\text{in}} + R_{\text{out}}}{2} \tag{3}$$

In (3), R_{in} and R_{out} are machine inner and outer radius, respectively. Therefore, r can be rewritten as:

$$r = \frac{g_{\max} - g_{\min}}{2} \tag{4}$$

The air gap length at mean radius R_{mid} can be expresses as follows [11]:

$$g_m(\theta) = g_0\Big(1 - SEF\ \cos(\theta - \gamma_0)\Big) \tag{5}$$

where θ is the angular stator position measured from a reference point (γ_0) of the minimal air gap. According to Figure 2b, the air gap length in all positions of (R,θ) can be calculated as [11]:

$$g(R,\theta) = g_m(\theta) - g'(R,\theta) \tag{6}$$

$$g'(R,\theta) = \big(R - R_{\min}\big)\ \sin\beta\ \cos(\theta - \gamma_0) \tag{7}$$

$$g(R,\theta) = g_0\left(1 - \frac{R}{R_{\text{mid}}} SEF\ \cos(\theta - \gamma_0)\right) \tag{8}$$

According to equation (8), in static eccentric condition, the air gap length varies from small to large around the circumference of the stator (sinusoidal variation), but the minimum air gap position is not time-variant as shown in Figure 3a. The dynamic eccentricity is also caused by the declined rotor plane, but the rotor axis is matched by the configuration presented in Figure 2c. In this case, a time-dependent sinusoidal variation of air gap will be created as shown in Figure 3b.

Figure 3b shows that in dynamic eccentricity, the air gap length is dependent on rotor angular velocity ($\omega_r = \frac{\omega}{p}$ where ω is the fundamental frequency in rad/s and p is the number of pole pairs). The dynamic eccentricity factor (DEF) is defined as static eccentricity, described in (1). Thus, the equation of dynamic eccentricity can be deduced with respect to equation (8) as follows [35]:

$$g(R,\theta) = g_0\left(1 - \frac{R}{R_{\text{mid}}} DEF\ \cos\left(\theta - \frac{\omega t}{p} - \gamma_0\right)\right) \tag{9}$$

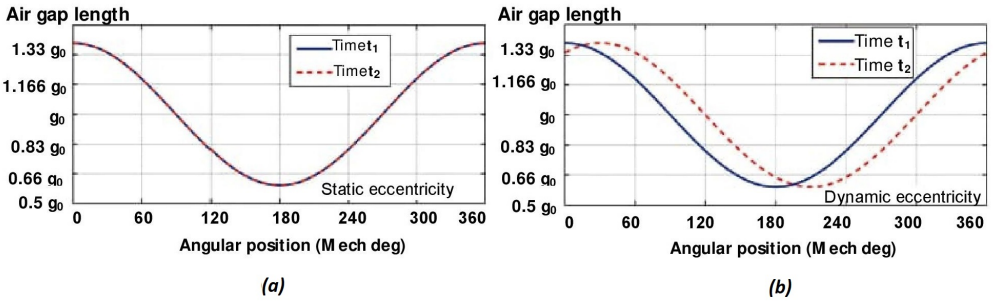

Figure 3. The change of air gap length: (a) static eccentricity condition, (b) dynamic eccentricity condition.

To introduce a frequency pattern of the stator current spectrum under dynamic eccentricity condition, the determination of air gap field components and subsequently permeance function in the faulty AFPM generator is necessary.

2.2. Permeance function

For explaining the basic concept of the proposed method, an analytical approach is first reviewed. In this analysis, the permeability of the iron is assumed to be infinite and flux fringing and leakage are neglected. In

AFPMs the length of magnets should be included in air gap length. So, the permeance function $p_{DE}(R,\theta)$ in permanent magnet machines can be written as [11]:

$$p_{DE}(R,\theta) = \frac{\mu_0}{g''(R,\theta)} \tag{10}$$

Where μ_0 is the permeability of air and $g''(R,\theta)$ is the air gap length under eccentric condition including the magnet length that can be expressed as:

$$g''(R,\theta) = g(R,\theta) + \frac{h_p}{\mu_{rc}} \tag{11}$$

where h_p is the magnet length and $\mu_r c$ is the permanent magnet recoil permeability, which is assumed to be 1. Therefore, the $g^{''}(R,\theta)$ can be written as $g(R,\theta)+h_p$ and dynamic eccentricity permeance function $p_{DE}(R,\theta)$ in AFPMs can be expressed as:

$$\begin{aligned} p_{DE}(R,\theta) =& \frac{\mu_0}{h_p + g(R,\theta)} \\ =& \frac{\mu_0}{h_p + g_0\left(1 - \frac{R}{R_{\text{mid}}} DEF\, \cos\left(\theta - \frac{\omega t}{p} - \gamma_0\right)\right)} \\ =& \frac{\frac{\mu_0}{h_p+g_0}}{1 - \frac{g_0 R}{(h_p+g_0)\, R_{\text{mid}}} DEF\, \cos\left(\theta - \frac{\omega t}{p} - \gamma_0\right)} \end{aligned} \tag{12}$$

It is assumed that $\frac{\mu_0}{(h_p+g_0)\, R_{\text{mid}}} DEF = h_0$ and $\frac{g_0 R}{(h_p+g_0) R_{\text{mid}}} DEF = h_m$. Thus, the air gap permeance is expressed as:

$$p_{DE}(R,\theta) - \frac{h_0}{1 - h_m\, \cos\left(\frac{\omega t}{p} - \theta - \gamma_0\right)} \tag{13}$$

The equation (13) can be presented as a Fourier series as [37]:

$$p_{DE}(R,\theta) = \frac{h_0}{\sqrt{1-h_m^2}} + \frac{2h_0}{\sqrt{1-h_m^2}} \times \sum_{k=1}^{\infty} \left\{ \left(\frac{1-\sqrt{1-h_m^2}}{h_m} \right)^k \cos k \left(\frac{\omega t}{p} - \theta - \gamma_0 \right) \right\} \tag{14}$$

The Equation (14) will be applied for the analytical justification of the proposed method in this section.

2.3. Air gap field components

Since one stator electrical fundamental period generates only $\frac{1}{p}$, a rotation for a p pole pairs AFPM, and the position of minimum air gap varies with the rotor rotation, magnetic flux density, winding inductances and the flux linkage will be different in $\frac{1}{p}$ of the rotation compared to other $\frac{p-1}{p}$ of rotation. The stator air gap field due to Ampere's law can be expressed as:

$$B_S(\theta,t) = p(R,t) \int \mu_0 j_S(\theta,t)\, \mathrm{d}\theta \tag{15}$$

where $j_S(\theta,t)$ is the current density on the stator surface and is defined as:

$$j_S(\theta,t) = J_S \sin(\omega t - \theta) \tag{16}$$

where J_S is the peak value of the surface current density. Stator air gap field can be expressed by combining (14)–(16) as:

$$B_S(\theta,t) = \left(\frac{h_0}{\sqrt{1-h_m^2}} + \frac{2h_0}{\sqrt{1-h_m^2}} \times \sum_{k=0}^{\infty} \left\{ \left(\frac{1-\sqrt{1-h_m^2}}{\mathrm{h_m}} \right)^k \cos k \left(\frac{\omega t}{p} - \theta - \gamma_0 \right) \right\} \right) \times \int \mu_0 \, J_S \sin(\omega t - \theta) \, \mathrm{d}\theta \tag{17}$$

Equation (17) can be simplified as follows:

$$B_S(\varphi,t) = \left(\frac{h_0}{\sqrt{1-h_m^2}} + \frac{2h_0}{\sqrt{1-h_m^2}} \times \sum_{k=0}^{\infty} \left\{ \left(\frac{1-\sqrt{1-h_m^2}}{\mathrm{h_m}} \right)^k \cos k \left(\frac{\omega t}{p} - \theta - \gamma_0 \right) \right\} \right) \times (\mu_0 J_S \cos(\omega t - \theta)) \tag{18}$$

Equation (18) can be rewritten as:

$$B_S(\varphi,t) = \left(\frac{\mu_0 h_0 J_S}{\sqrt{1-h_m^2}} \cos(\omega t - \theta) + \frac{2\,\mu_0 h_0 J_S}{\sqrt{1-h_m^2}} \times \sum_{k=0}^{\infty} \left\{ \left(\frac{1-\sqrt{1-h_m^2}}{\mathrm{h_m}} \right)^k \cos k \left(\frac{\omega t}{p} - \theta - \gamma_0 \right) \cos(\omega t - \theta) \right\} \right) \tag{19}$$

By multiplying the cosine statements in the parentheses, equation (19) can be presented as:

$$B_S(\varphi,t) = \frac{\mu_0 h_0 J_S}{\sqrt{1-h_m^2}} \cos(\omega t - \theta) + \frac{\mu_0 h_0 J_S}{\sqrt{1-h_m^2}} \times \left\{ \sum_{k=0}^{\infty} \left(\frac{1-\sqrt{1-h_m^2}}{\mathrm{h_m}} \right)^k \times \left[\cos\left(\left(1 - \frac{K}{P} \right) \omega t + K\gamma_0 + (K-1)\theta \right) + \cos\left(\left(1 + \frac{K}{P} \right) \omega t - K\gamma_0 - (K+1)\theta \right) \right] \right\} \tag{20}$$

To determine a definition for the rotor MMF wave components, it is assumed that $\theta = \omega t + \theta'$ and a similar survey can be performed for rotor air gap field. Therefore, the air gap field can be expressed as follows:

$$B(t) = B_0 \cos(\omega t - \theta_0) + \left\{ \sum_{k=0}^{\infty} B_k \left[\cos\left(\left(1 - \frac{K}{P} \right) \omega t - \theta_1 \right) + \cos\left(\left(1 + \frac{K}{P} \right) \omega t - \theta_2 \right) \right] \right\} \tag{21}$$

The MMF considering eccentricity fault can be defined as $F(t) = B(t)\,g(t)$. Thus, the air gap field components raise in the current spectrum, and it is expected that the subharmonics at frequencies $\left(1 \pm \frac{K}{P}\right) f_s$, ($f_s$ is the fundamental frequency and k is an integer number) can be introduced as proper signatures for eccentricity fault diagnosis, but it is noticeable that in addition to fault impacts, the current frequency pattern affected by different factors such as design characteristics, the winding configuration and even the manufacturing procedure. In order to remove such harmonic components from the aforementioned frequency pattern, the

sideband components at odd coefficients ($K = 1, 3, 5, \cdots$.) is proposed as a competent criterion for dynamic eccentricity fault diagnosis ($f_{DE} = \left(1 \pm \frac{2k-1}{P}\right) f_s$) [37]. To validate this analytical approach, an axial flux permanent magnet generator with 5 pole pairs has been studied. Since the main field generates fundamental harmonic at frequencies 50 Hz, it is expected that the dynamic eccentricity causes current components at frequencies of 40 Hz and 60 Hz ($2k-1=1$), 20 Hz and 80 Hz ($2k-1=3$), 100 Hz ($2k-1=5$), 120 Hz ($2k-1=7$), 140 Hz ($2k-1=9$), 160 Hz ($2k-1=11$). The current components caused by dynamic eccentricity condition are extracted by Hilbert-Huang transform, as introduced in the next section.

2.4. Axial unbalanced magnetic force due to eccentricity

The axial magnetic force between the rotor and the stator is very high; therefore, a slight rotor dissymmetry could cause an unbalanced magnetic pull (UMP) and, consequently, induce vibration. The magnetic forces produced by PMs comprise the normal F_n and tangential F_t components and are computed using Maxwell's stress tensor as follows [38]:

$$F_n = \frac{1}{2\mu_0}\left[\sum_{j}^{N}\left(B_{nj}^2 - B_{tj}^2\right)\right] \tag{22}$$

$$F_t = \frac{1}{\mu}\left[\left(\sum_{j}^{N} B_t^2\right)\right] \tag{23}$$

where B_n and B_t are normal and tangential components of magnetic flux density and $j = 1, 2, 3, \ldots, N$. While F_t produces the useful electromagnetic torque, F_n causes the vibration and noise of electromagnetic origin. As described above, the SE fault has significant effects on the air gap flux pattern and consequently leads to electromagnetic harmonic component, which is present in the vibration spectrum. In other words, under eccentricity condition, the air gap varies in axial length from small to large around the circumference of the stator. Therefore, the permeance varies axially across the machine circumference from maximum to minimum in the regions of minimum to maximum air gap, respectively, and the flux density is increased due to minimum reluctance of the magnetic circuit but gradually decreased across the remaining part of the air gap. Since B_{nj} in (22) is a product of the air gap MMF and air gap permeance, in nonuniform permeance, the rotating air gap MMF becomes asymmetric, thereby exciting the harmonics j, which, when interacted with each other and/or armature reaction fields, may incite F_n and other electromagnetic harmonics and, consequently, induce vibration of the stator and machine housing. The axial magnetic force due to eccentricity can be expressed as [39]:

$$\begin{aligned} F_{z\_dyn} = & \frac{W_{tooth}}{4\mu_0} \times \frac{h_{PM}s}{\theta_{skew}}\left\{\cos\left(\frac{\theta_{skew}}{h_{PM}}\left(h_{PM} - h_{tooth}\right)\right) - 1\right\} \\ & \times \sum_{n=1}^{s}\sum_{k=1}^{\infty}\sum_{l=1}^{\infty}\sum_{m=1}^{\infty} B_k B_l \sin\left(ms\omega t - \left(\phi_k + \phi_l \pm m\partial\right)\right) \end{aligned} \tag{24}$$

where θ_{skew}, B_k (B_l), ϕ_k (ϕ_l), and ∂ are rotor skew angle, amplitude of magnetic flux density components, phase of the magnetic flux density and the magnitude of eccentricity. The W_{tooth}, h_{PM}, s, and h_{tooth} are the constant values related to machine parameters.

3. Dynamic eccentricity diagnosis based on Hilbert-Huang transform

The Hilbert-Huang transform (HHT) is the expansion of the Hilbert transform for nonlinear and nonstationary signal analysis. The HHT consists of two parts: empirical mode decomposition and Hilbert spectral analysis (HSA). EMD is applied to decompose the main signal into monotonic frequency components, known as intrinsic mode function (IMF). The obtained signatures of Hilbert transform of the IMFs is used as features for fault diagnosis. This section presents the use of HHT for axial flux generator stator currents analysis in nonstationary conditions.

3.1. Empirical mode decomposition

The applications of the Hilbert transform are all limited to monocomponent functions with only one frequency value at any given time; hence, the (EMD) method is necessary to deal with multicomponent signals from nonstationary and nonlinear processes. The EMD is basically defined by an algorithm, as in the following steps [40]:

1. Identification of all extrema (local minima and local maxima points) of actual signal x[n].
2. Connecting all local minima (resp. all local maxima) to produce the lower and upper envelope ($e_{min}[n]$ and resp. $e_{max}[n]$).
3. Extraction of the mean as
$$m[n] = \frac{e_{min}[n] + e_{max}[n]}{2} \tag{25}$$
4. Computation of the detail as
$$d[n] = x[n] - m[n] \tag{26}$$
5. Algorithm iteration by considering $d[n]$ instead of $x[n]$ (sifting process).

The algorithm has to be refined by repeating the sifting process until two conditions are fulfilled [40]:

1. The quantity of extrema and the quantity of zero-crossings should either equal or differ at most by one.
2. The mean value of the lower and upper envelopes should be close to zero.

After this procedure, the detail $d[n]$ corresponds to the first Intrinsic Mode Function (IMF1) which is named c_1, and the residue r_1 is defined as

$$r_1[n] = \mathrm{x}[n] - c_1[n] \tag{27}$$

r_1 is treated as the new actual data (instead of $x[n]$) and subjected to the same sifting process as described above. This procedure is repeated to extract more IMFs. The sifting process can be stopped finally by any of the following predetermined criteria: 1. when the component $C_i[n]$ or the residue $r_i[n]$ becomes so small that it is less than the predetermined value of substantial consequence; or 2. when the residue $r_i[n]$ becomes a monotonic function from which no more IMFs can be extracted.

3.2. Instantaneous amplitude (IA) and frequency (IF) extraction by the Hilbert transform (HT)

The IA and IF of each IMF are computed using the Hilbert transform. When the EMD is jointly applied with the Hilbert transform, the transformation is named the HHT. The discrete definition of the Hilbert transform is formulated as

$$x^h[n] = x[n] * h[n] \tag{28}$$

where $*$ points the convolution product. The superscript in $X^h[n]$ denotes the Hilbert transform of the sampled stator current $x[n]$, and

$$h[n] = \begin{cases} 0 & \text{for even } n \\ \frac{2}{n}\pi & \text{for odd } n \end{cases} \tag{29}$$

The analytic signal is defined as

$$z^h[n] = x[n] + jx^h[n] = a[n]e^{j\varphi[n]} \tag{30}$$

The instantaneous amplitude (IA) and the instantaneous frequency (IF) are given by

$$\hat{a}[n] = \left|z^h[n]\right| \tag{31}$$

$$\hat{f}[n] = \frac{1}{2\pi}\left(\angle\left(z^h[n+1]\right) - \angle\left(z^h[n]\right)\right) \times F_s \tag{32}$$

where $\left|z^h[n]\right|$ and $\angle\left(z^h[n]\right)$ are the modulus and the argument of complex-valued signal $z^h[n]$, respectively, and F_s is the data sampling rate. Finally, the time-frequency distribution is obtained by displaying the time evolution of the instantaneous amplitude and frequency for each IMF in the time-frequency plane.

3.3. HHT-based algorithm for eccentricity diagnosis in AFPMs

The proposed procedure for dynamic eccentricity diagnosis in AFPMs is represented by Figure 4. The fault components will be derived by means of EMD in the presence of dynamic eccentricity. After signal decomposition to its components, the Hilbert transform is used to compute the instantaneous amplitude (IA) and the instantaneous frequency (IF) of each IMFs. In fact, the Hilbert transform converts the local energy and IF extracted from the IMFs to full-energy-frequency-time distribution of the signal, with energy defined as the amplitude squared [41]. The signal energy is represented by the joint function of time and the IF. Such a representation is named Hilbert spectrum. The more significant IMFs caused by faulty conditions are determined by means of Hilbert spectrum, which are considered as dynamic eccentricity indicators.

4. Simulation and experimental results

In order to validate the usefulness of the proposed method, simulations and experiments have been carried out on a double-sided AFPM generator (Figures 5a and 5b) in healthy and faulty states under various conditions. In the experimental setup, dynamic eccentricity is caused by the declined rotor plane, which can be implemented by changing the position of the rotor discs. This is done via axial bolts that can be seen on the picture in Figure 5c. A fillet gauge was applied to measure the resulting g_{max} and g_{min} to ensure accuracy. Because of the high ratio of machine diameter to length in the AFPMs, *DEF* of more than 40% is not considered in this study. The experimental setup for data sampling, including AC motor (with speed control drive), AFPM

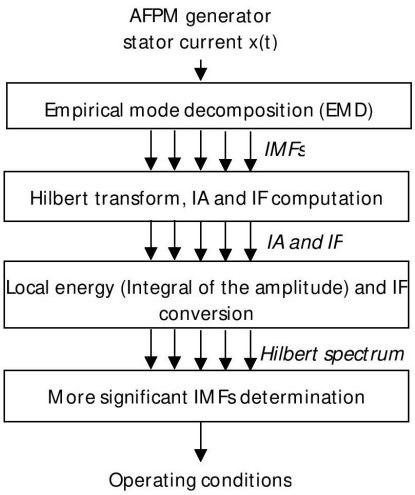

Figure 4. The proposed algorithm for dynamic eccentricity diagnosis in AFPMs.

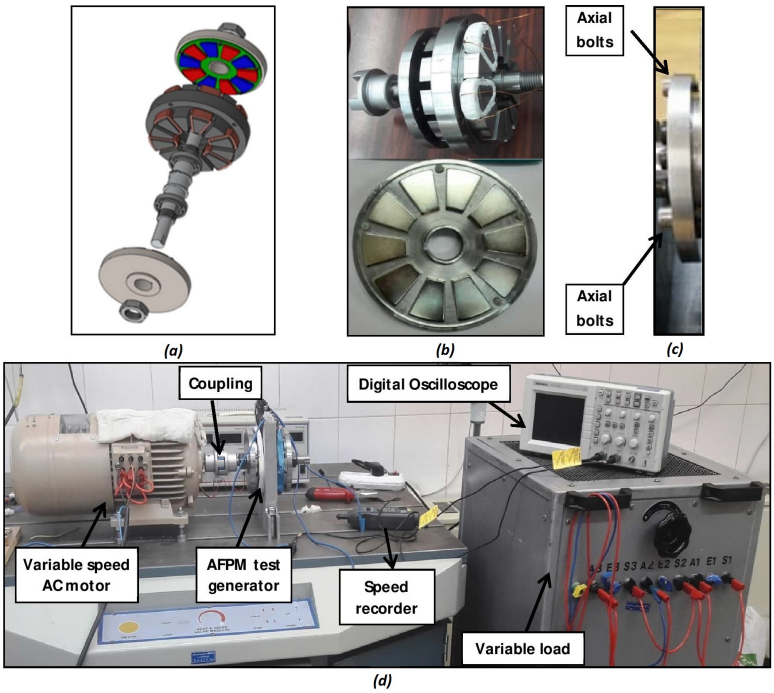

Figure 5. (a) Exploded view drawing of axial flux permanent magnet test generator, (b) stator core with two installed coils and rotor disk with PM pieces, (c) declined rotor implemented by axial bolts, (d) practical setup for experimental data sampling.

generator, oscilloscope, and variable load is shown in Figure 5d. The constructed generator characteristics are listed in Table 1.

Moreover, the 3D-FEM is used for the simulation of the test generator, which is carried out through the Maxwell FEM software. The simulated AFPM generator under eccentricity condition with linear and nonlinear load is shown in Figure 6. The "Rotate Operator" in Maxwell FEM software is applied to make a small deviation angle of the rotor coordinate system around the y-axis for DE fault simulation. In this case, the rotor rotates

Table 1. AFPM generator characteristics table.

Phase EMF (RMS) @ 600rpm	**81.42**	**V**
Outer diameter of stator	132	mm
Inner diameter of stator	25	mm
Air gap length	1.2	mm
Machine mechanical rated speed	500	rpm
Number of coils per each side of stator	6	
Number of coils on double-sided stator	12	
Number of PM pieces per each rotor disk	10	
Number of PM pieces in generator	20	
Electrical frequency	50	Hz
Rated phase current (RMS)	1.2	A
Rated output power	100	W
Number of conductor turns per coil	180	
Conductor diameter	0.55	mm
PM pieces class	N52 MGOe	
Magneto motive Force of PM pieces	923000	At

around the z-axis of the stator coordinate system, as detailed in Figure 2c. The nonuniform air gap caused by DE fault is seen in Figure 6a. When the simulated AFPM is running under nonstationary faulty condition, phase current sampling is achieved through Maxwell software at 10 kSample/s sampling rate and the phase current data is saved in a CSV file which makes it possible to process the phase current data based on proposed method.

Experimental current data acquisition is carried out by using a digital oscilloscope with nominal sampling rate of 1000 kSample/s, as detailed in Figure 5d. The experimental data is transferred from digital oscilloscope to personal computer expert diagnosis through a USB data cable and is saved in a CSV file, which allows data to be saved in a table structured format in plain text. Each line of the CSV file is a recorded data and each record consists of one field separated. The FEM simulations and experimental current data are processed based on Hilbert-Huang transform through MATLAB software in personal computer expert diagnosis. The experimental results are compared to those of the simulation tests and the expectations of theoretical analysis.

For a comprehensive method survey, a set of simulations and experiments have been carried out at unsteady speed with linear and nonlinear load under healthy and eccentricity conditions of generator with DEF=26% and DEF=40%. In the case of simulations and experiments, g_{min} and g_{max} are set on 0.88 mm and 1.51 mm, respectively, for DEF=26%, and also g_{min} and g_{max} are set on 0.72 mm and 1.68 mm respectively for DEF=40%. The actual and simulated stator currents have been recorded for 3.5 s with a 10 kHz sampling rate as shown in Figures 7a and 7b.

Figure 7c gives a series of computed IMFs extracted from the original signal of actual generator under eccentricity condition with DEF=40% at speed variations of 0% to nominal speed in the presence of a linear load. These IMFs have been generated at frequencies $\left(1 \pm \frac{2K-1}{P}\right) f_s$ (20 Hz, 40 Hz, 60 Hz, 80 Hz, 120 Hz, 140 Hz, 160 Hz, 180 Hz, 200 Hz, and 220 Hz at nominal speed) due to dynamic eccentricity fault. The more significant IMFs caused by faulty condition are determined by means of Hilbert spectrum, which are applied for dynamic eccentricity identification.

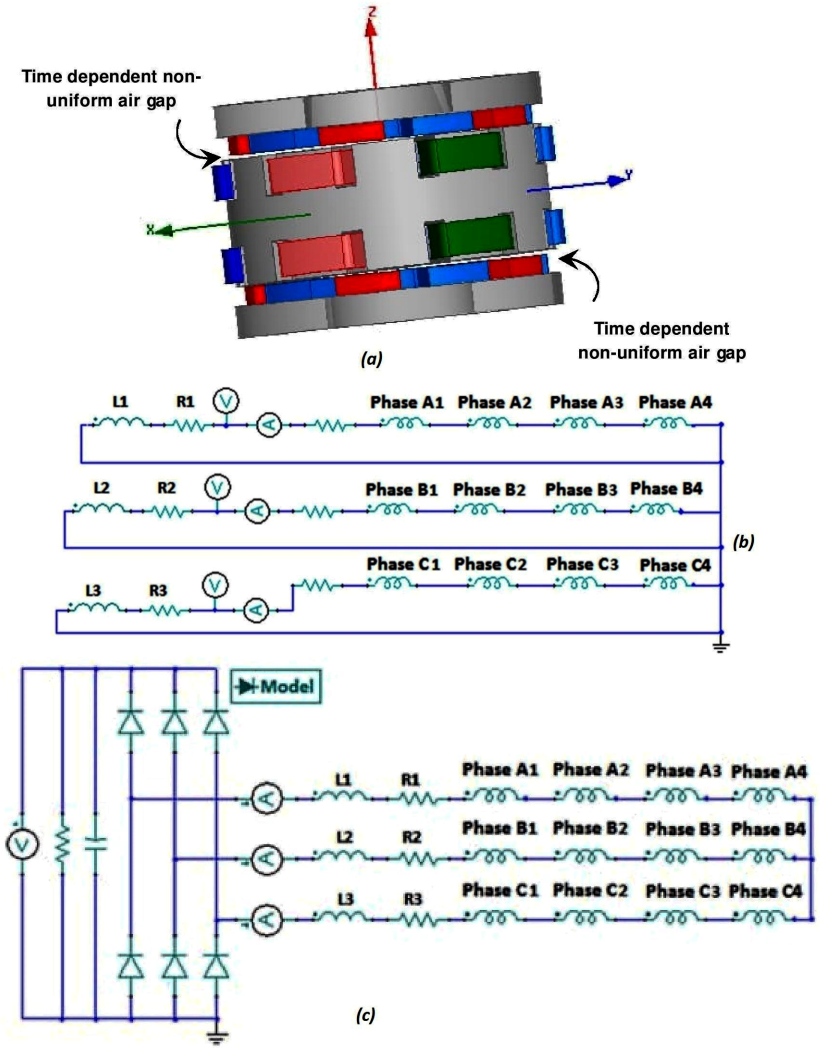

Figure 6. (a) Simulated AFPM generator under eccentricity condition in Maxwell FEM software, (b) simulated linear load in Maxwell FEM software, (c) simulated nonlinear load in Maxwell FEM software.

For instance, Figure 8 gives the Hilbert spectrum of stator current under healthy and eccentricity conditions at speed variations of 0% to nominal speed in the presence of a linear load. The colour bar in Hilbert spectrum presents energy levels in A^2 (amplitude squared). The amplitude of fault components is small in comparison to the amplitude of the fundamental harmonics; thus, to increase the resolution of T-F (time–frequency) distributions, the fundamental, 3rd, 5th, and 7th harmonics have been removed by EMD and cannot be seen on IMF1 to IMF11. It makes the appearance of fault components in Hilbert spectrum easier. As shown in Figures 8a and 8b, only the fundamental and subharmonics (3rd, 5th, and 7th) can be seen in the Hilbert spectrum under healthy conditions and no fault components have appeared. Figures 8c and 8d show the energy of IMFs affected by dynamic eccentricity under simulated and actual fault condition, with DEF=40%.

Table 2 gives the instantaneous frequency (IF) of simulated and experimental stator current components under dynamic eccentricity condition with *DEF=26%* and *DEF=40%* in the presence of a linear load. The table is divided into four subsets based on the various generator speeds at 50, 150, 300, and 500 RPM. The phase

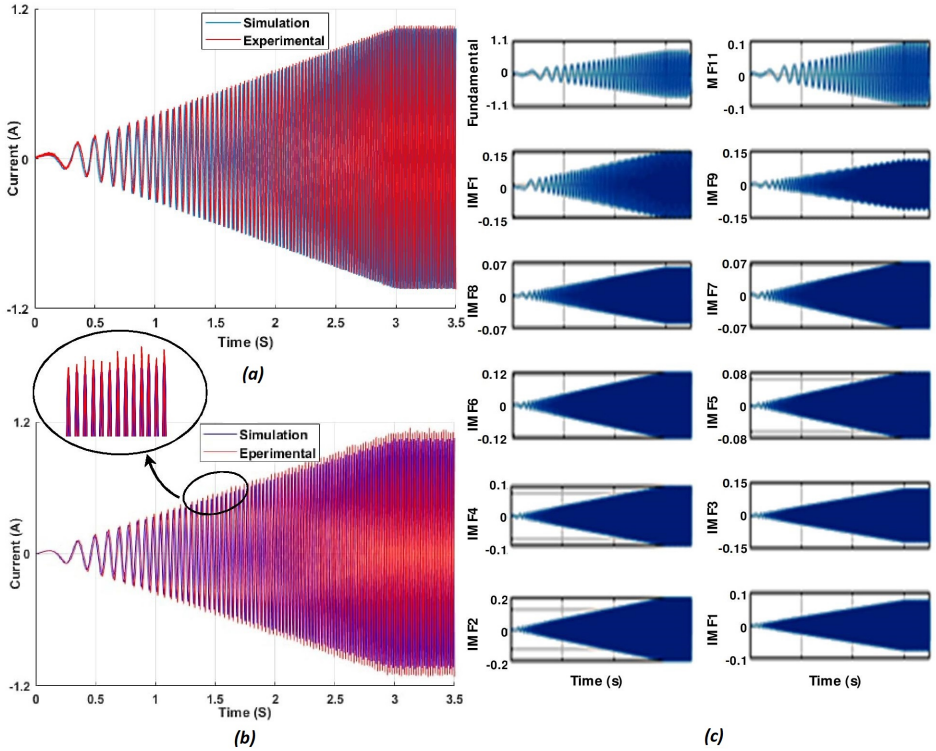

Figure 7. Simulated and experimental stator current (linear load): (a) healthy condition, (b) eccentricity condition (DEF=40%), (c) a series of computed IMFs under actual eccentricity condition (DEF=40%).

currents are sampled at different speed and fault severity to obtain the frequency spectrum of phase currents using Hilbert-Huang transform.

As it can be seen in the table, in addition to the fundamental component and its harmonics, the current components at frequencies $\left(1 \pm \frac{2K-1}{P}\right) f_s$ (The instantaneous fundamental frequency depends on instantaneous rotor speed) will appear together in the presence of dynamic eccentricity. Figures 9a–9d give the energy values of the simulated and experimental stator current components under eccentricity condition with DEF=26% and DEF=40% in the presence of a linear load. The faulty condition is decomposed into four parts at 10%, 30%, 60%, and 100% of nominal speed. The energy value is defined as the amplitude squared multiplied by 10^{+6}.

As it can be seen in Figures 9a–9d, the HHT allows removing the undesired frequencies in both an easy and fast way. It makes it possible to observe the more important IMFs individually to increase the precision in the fault diagnosis. As shown, the energy of fault components increases with respect to fault severity. Moreover, it seems that the 2nd and 10th IMFs are the most affected IMFs and the energy of these IMFs is more reliable as fault indicator and its severity at different rotor speed.

Accurate fault diagnosis is questionable without investigating the relations between the load conditions and current frequency pattern. Therefore, further results are presented here to validate the proposed technique in the presence of a nonlinear load. Based on the aforementioned proved formula, the number of poles and supply frequency (depends on rotor speed) change the fault components. The same frequency components that are affected by dynamic eccentricity may be introduced by nonlinear loads, so some harmonics can be observed in both healthy and eccentricity conditions.

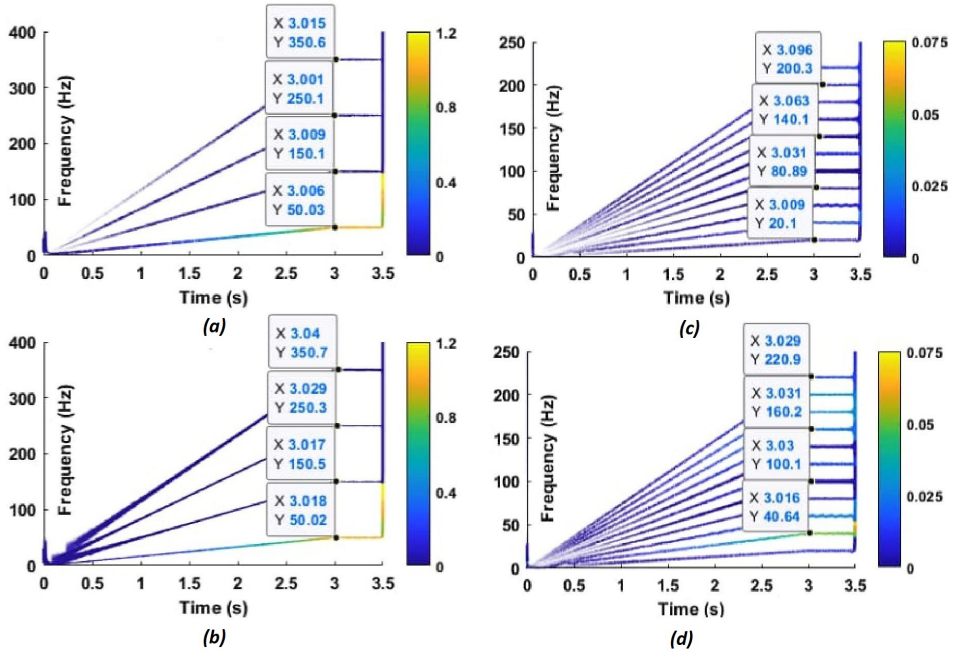

Figure 8. Hilbert spectrum of stator current (linear load): (a) simulated healthy condition, (b) actual healthy condition, (c) simulated eccentricity condition (DEF=40%), (d) actual eccentricity condition (DEF=40%).

Figures 10a and 10b give the simulated and experimental stator current at unsteady speed with a nonlinear load under healthy and eccentricity conditions of generator with DEF=40%. The Hilbert spectrum of experimental stator current under healthy condition is shown in Figure 10c. As seen, the presence of nonlinear load leads to harmonics (2nd, 11th, 13th, and 15th) associated with the switching operation of the converters. The amplitude of switching harmonics is small in comparison to the amplitude of the fundamental component; thus, to increase the resolution of T-F distributions, the fundamental harmonic has been removed by EMD and cannot be seen in Hilbert spectrum. Figure 10d shows the fault components of experimental stator current in Hilbert spectrum under eccentricity condition with *DEF=40%*. As shown in Figure 10d, the EMD process does clear the signal from the effects of switching operation in nonlinear loads for reliable and accurate fault identification.

Table 3 gives instantaneous frequency (IF) of the simulated and experimental stator current components under eccentricity condition with DEF=26% and DEF=40% in the presence of a nonlinear load. As it can be seen in the table, in addition to fundamental component and switching harmonics, the current components at frequencies $\left(1\pm\frac{2K-1}{P}\right) f_s$ (The instantaneous fundamental frequency depends on instantaneous rotor speed) will appear together in the presence of dynamic eccentricity.

Figures 11a–11d give the energy values of the simulated and experimental stator current components under eccentricity condition with DEF=26% and DEF=40% in the presence of a nonlinear load. The faulty condition is decomposed into four parts at 10%, 30%, 60%, and 100% of nominal speed. Similar to the linear load conditions, current frequency pattern is speed-dependent and the components energy values increase almost linearly with respect to the speed and fault severity.

As it has been demonstrated in this section, under nonstationary conditions with linear or nonlinear load, the stator current would have to be filtered by means of the EMD to remove the fundamental and other

Table 2. The instantaneous frequency of the simulated and experimental stator current components under eccentricity conditions in the presence of a linear load

operating speed / nominal speed			Stator current components															Instantaneous frequency (IF) (Hz)
			harmonics				IMFs											
			Fund	3rd	5th	7th	IMF 1	IMF 2	IMF 3	IMF 4	IMF 5	IMF 6	IMF 7	IMF 8	IMF 9	IMF 10	IMF 11	
DEF=40%	Simulation	10%	4.82	15.01	25.04	34.83	1.8	4.03	6.13	7.91	70.12	12.32	13.91	16.12	17.89	19.91	22.13	
		30%	15.08	44.83	75.46	104.71	6.13	12.09	17.82	24.12	29.88	35.92	42.06	48.01	53.93	60.21	66.07	
		60%	30.53	90.21	149.83	210.41	12.02	23.96	35.87	48.08	60.13	72.3	83.97	96.07	107.82	120.23	121.9	
		100%	50.23	150.2	250.3	350.17	20.1	40.08	60.03	80.89	100.15	120.4	140.1	160.0	180.23	200.3	220.4	
	Experimental	10%	5.31	14.71	24.73	35.07	1.76	4.41	5.97	8.04	10.23	12.42	14.07	16.31	18.05	20.53	22.41	
		30%	15.47	45.13	74.62	105.35	6.03	12.12	18.23	23.87	30.05	35.61	42.21	47.74	54.24	60.36	66.17	
		60%	29.62	89.21	150.51	210.17	11.91	24.36	36.04	47.86	60.47	71.81	84.09	96.43	108.37	119.73	121.7	
		100%	50.14	150.3	250.2	350.47	19.82	40.64	59.81	80.49	100.1	120.3	139.6	160.2	179.3	199.34	220.9	
DEF=40%	Simulation	10%	4.53	15.28	25.39	34.63	2.34	3.81	6.34	8.24	9.73	11.85	14.26	15.83	17.63	20.37	21.68	
		30%	15.23	44.56	74.91	105.47	6.28	11.73	18.37	23.51	29.69	36.08	41.82	47.59	54.39	60.06	66.35	
		60%	30.31	90.44	150.23	209.62	11.63	23.41	36.27	48.36	60.17	72.13	83.71	96.14	107.63	119.53	122.3	
		100%	50.31	150.1	250.4	350.29	20.04	39.73	59.63	80.99	99.74	120.1	140.1	159.7	180.1	200.3	219.6	
	Experimental	10%	4.74	15.53	24.61	35.36	1.7	4.26	5.63	7.74	10.34	11.71	13.61	16.43	18.68	19.61	21.76	
		30%	14.57	45.41	75.39	104.63	5.64	12.41	17.56	24.41	30.14	36.49	42.36	48.38	53.74	59.57	65.67	
		60%	29.58	90.25	149.62	210.27	12.32	24.17	35.51	47.62	59.73	72.1	84.24	95.66	108.32	119.81	122.4	
		100%	49.84	149.9	250.1	350.38	19.64	40.39	59.77	79.56	100.1	119.6	139.7	160.1	180.2	200.14	220.9	

subharmonics prior to the applications of the fault diagnosis algorithm. This filtering increases the resolution of TF distributions and makes the identification of fault metrics easier.

The presented approach can be extended to discriminate the SE, DE, and ME faults. In order to simulate the static eccentricity, rotor coordinate system is deviated as much as β around y-axis by "Rotate Operator" in Maxwell FEM software. In this case, the rotor rotates around the z-axis of its own coordinate system, as detailed in Figure 2b.

Figures 12a and 12b give the energy values of the simulated stator current components under static eccentricity condition with SEF=26% and SEF=40% in the presence of a linear load. The faulty condition is decomposed into two parts at 60% and 100% of nominal speed. The energy value is defined as the amplitude squared multiplied by 10^{+6}.

As shown in Figures 12a and 12b, SE fault generates sideband components at frequencies $\left(1\pm\frac{2K-1}{P}\right)f_s$. Thus, the amplitude of sideband components of the aforementioned pattern frequency can be applied for the detection of SE. Meanwhile, Figures 12a and 12b show that a higher degree SE increases the amplitude of sideband components at frequencies $\left(1\pm\frac{2K-1}{P}\right)f_s$ considerably. It is noticeable that the incremental rate of the SE degree is sharper than that of the DE fault. Therefore, it is possible to discriminate the SE and DE faults using the difference between the amplitude of sideband components at frequencies $\left(1\pm\frac{2K-1}{P}\right)f_s$.

If both of rotor and stator coordinate systems are deviated as much as different angles around the y-axis and the rotor rotates around the z-axis of the stator coordinate system, the ME fault is simulated. In other words, under ME condition, the symmetrical axis of the rotor and stator and the rotation axis of the rotor are

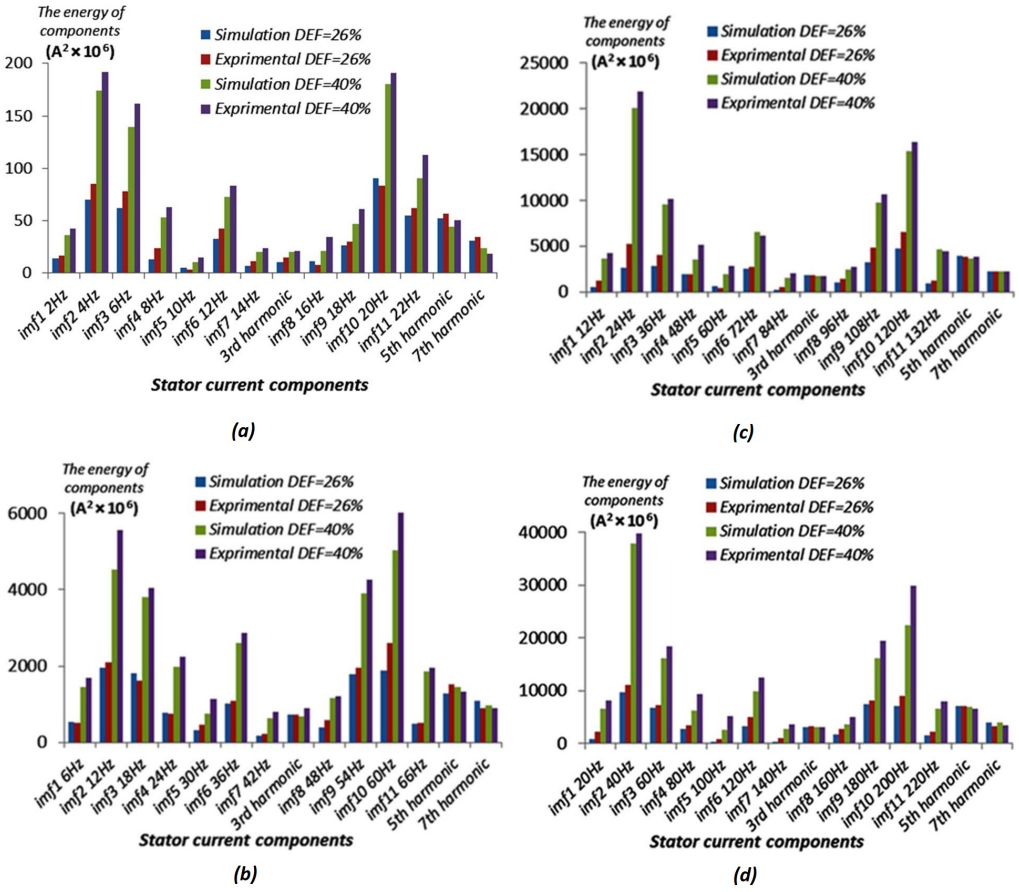

Figure 9. Current components under DE condition with a linear load (a) at 10% of nominal speed, (b) at 30% of nominal speed, (c) at 60% of nominal speed, (d) at nominal speed.

displaced. The spectrum energy of simulated AFPM with 25% SE and 20% DE, and 40% SE and 35% DE is shown in Figure 13. Referring to Figure 13, the incremental rate of amplitude of sideband components due to ME is more than that of the SE or DE case.

A comparison between the spectrum current of the faulty AFPM due to DE, SE, and ME fault illustrates that a hierarchical scheme can be employed for eccentricity fault classification and its severity. The first classifier only decides whether the eccentricity is ME or purely static or dynamic, and then, another classifier estimates the eccentricity severity according to its type. Thus, a k-NN classifier is employed for the diagnosis of the eccentricity fault type, and then, a multilayer perceptron artificial neural network (ANN) is applied for the estimation of eccentricity severity. The utilization of ANNs for pattern classification has been deeply studied in [42].

It is noticeable that k-NNs are a nonparametric classifier based on nonparametric estimation of the class densities. The simplest version of this algorithm is for $k = 1$. However, in most practical applications, the data distributions for various classes are overlapping, and more than one NN ($k > 1$) is applied for majority voting. As this classifier is well known for electrical machine fault detection [43], it can be employed for estimating the eccentricity type.

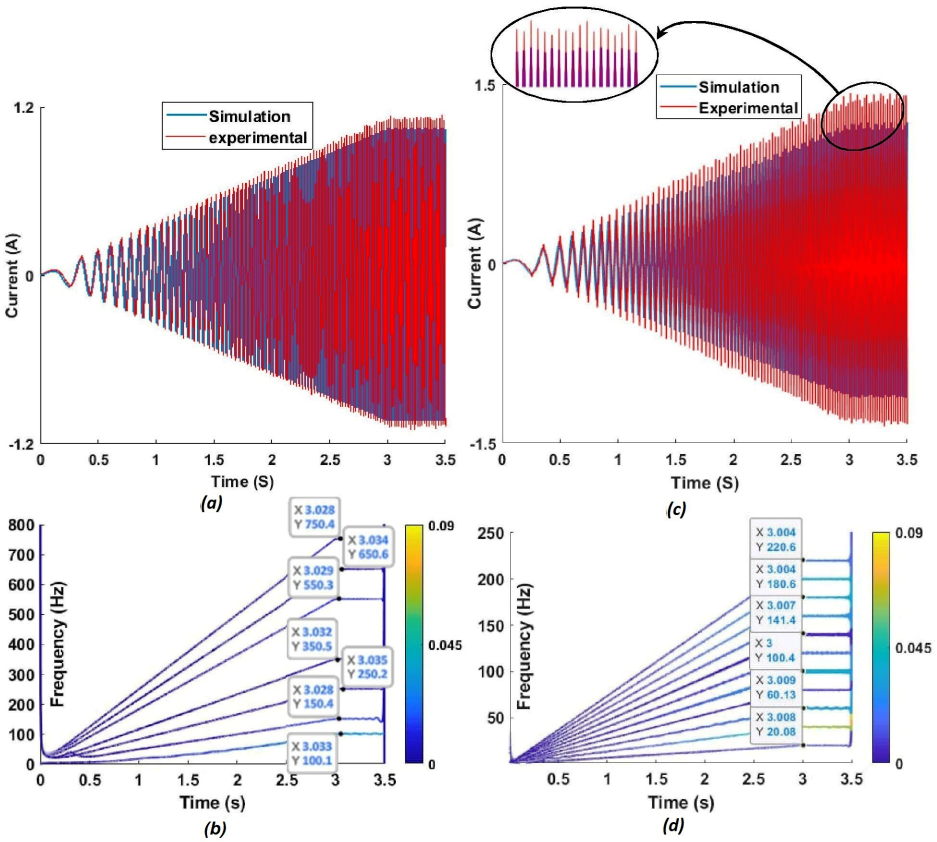

Figure 10. Simulated and experimental stator current (nonlinear load): (a) healthy condition, (b) eccentricity condition (DEF=40%), Hilbert spectrum of actual stator current, (c) healthy condition, (d) eccentricity condition.

5. Conclusion

The objective of this paper is to develop a new technique for dynamic eccentricity diagnosis in double-rotor double-sided stator structure AFPM generator. Since the traditional methods such as vibration, acoustic noise, magnetic field, and torque analysis are generally expensive, invasive, and complicated and can lead to incorrect diagnosis, the method was based on current signature analysis by means of Hilbert-Huang transform. As the variable load and speed can have significant effect on the proposed indices in any fault diagnosis, the most important requirement for the new method is sensitive detection of dynamic eccentricity under unsteady speed and load conditions, especially at the initial stages of the fault occurrence.

Firstly, the method was described by following an analytical approach to show that the frequency pattern of the stator current spectrum under dynamic eccentricity condition introduces appropriate indices for fault detection.

Secondly, the mathematical foundations of Hilbert–Huang transform were settled and the use of the HHT for proposed indices extraction was investigated, which makes the robust diagnosis against load and speed variations.

Thirdly, the analytical formulation of fault detection process was validated through both simulations and experiments. Sixteen scenarios with DEFs of 26% and 40% were considered at 10%, 30%, 60%, and 100% of nominal generator speed with linear and nonlinear load. In the 3D-FEM and experimental results, the average error in frequency of extracted current components affected by dynamic eccentricity, was less than 3.5% and

Table 3. IF of the simulated and experimental stator current components under eccentricity conditions in the presence of a nonlinear load.

operating speed / nominal speed			Stator current components															Instantaneous frequency (IF) (Hz)
			harmonics				IMFs											
			Fund	11th	13th	15th	IMF 1	IMF 2	IMF 3	IMF 4	IMF 5	IMF 6	IMF 7	IMF 8	IMF 9	IMF 10	IMF 11	
DEF=40%	Simulation	10%	4.88	55.23	64.71	74.75	1.88	4.14	6.26	8.05	10.29	12.51	14.11	16.35	18.13	20.17	22.42	
		30%	15.29	164.8	195.14	225.16	6.26	12.27	18.06	24.41	30.22	36.32	42.51	48.52	54.49	60.83	66.74	
		60%	30.28	330.4	390.53	450.34	12.15	24.14	36.10	48.36	60.46	72.67	84.39	96.54	108.3	120.8	122.5	
		100%	50.48	549.5	649.84	749.91	20.25	40.29	60.30	81.14	100.44	120.7	140.4	160.4	180.6	200.7	220.6	
	Experimental	10%	5.47	55.12	65.14	75.16	1.84	4.52	6.10	8.19	10.40	12.61	14.28	16.54	18.30	20.80	22.70	
		30%	15.39	165.2	195.27	225.31	6.16	12.30	18.47	24.16	30.40	36.01	42.67	48.25	54.80	60.98	66.84	
		60%	30.16	329.6	389.84	449.91	12.04	24.54	36.27	48.14	60.80	72.18	84.51	96.90	108.8	120.2	122.3	
		100%	5029	550.4	650.53	750.28	19.96	40.85	60.07	80.74	100.59	120.6	139.9	160.6	179.7	199.8	219.7	
DEF=40%	Simulation	10%	4.68	54.6	65.40	75.46	2.43	3.91	6.47	8.39	9.89	12.03	14.47	16.05	17.87	20.64	21.96	
		30%	15.48	165.4	195.53	225.38	6.41	11.91	18.61	23.80	30.03	36.48	42.27	48.09	54.96	60.68	67.02	
		60%	30.85	330.2	389.71	449.76	11.76	23.59	36.50	48.64	60.50	72.50	84.13	96.61	108.1	120.0	122.8	
		100%	50.26	550.1	650.14	750.17	20.19	39.93	59.89	81.24	100.02	120.4	140.4	160.1	180.5	200.7	219.8	
	Experimental	10%	4.79	55.45	65.53	75.61	1.78	4.37	5.75	7.88	10.51	11.89	13.81	16.66	18.93	19.87	22.04	
		30%	14.74	164.7	194.84	224.90	5.77	12.60	17.79	24.71	30.49	36.89	42.82	48.89	54.30	60.18	66.34	
		60%	29.96	329.9	390.14	450.17	12.45	24.35	35.74	47.90	60.05	72.47	84.66	96.13	108.8	120.3	122.2	
		100%	50.43	550.2	649.71	750.12	19.78	40.28	60.03	79.80	100.39	119.9	140.0	160.5	180.6	200.6	219.6	

4.5%, respectively, compared with the theoretical frequency of proposed indices. Moreover, in the experimental results, the average error in energy of the IMFs affected by dynamic eccentricity was less than 4%, compared with those of the 3D-FEM results.

The contributions of this paper are as follows:

1. Compared with existing eccentricity diagnosis method, the proposed method provides a more reliable and accurate evaluation of eccentricity fault occurrence when the stator currents are not absolutely sinusoidal due to the harmonics caused by nonlinear loads, in such a way that the applied technique makes the extraction of eccentricity signatures easier by rejecting the load related components and other undesired frequencies.

2. As the fault-related signatures at initial stages of the fault occurrence are very weak and also are chaotic due to load and speed variations, the proposed approach, in comparison to other MCSA methods, provides more robust diagnosis by tracking the faulty frequencies using effective HHT-based technique. Moreover, as shown in the diagrammatic presentation of results, the energy of the IMFs increases with respect to fault severity and the eccentricity degree can be evaluated based on the IMFs energy value.

The proposed approach could be developed to discriminate the SE, DE, and ME faults and also to detect several AFPMs faults signatures such as partial and uniform demagnetization and inter-turn short circuit faults.

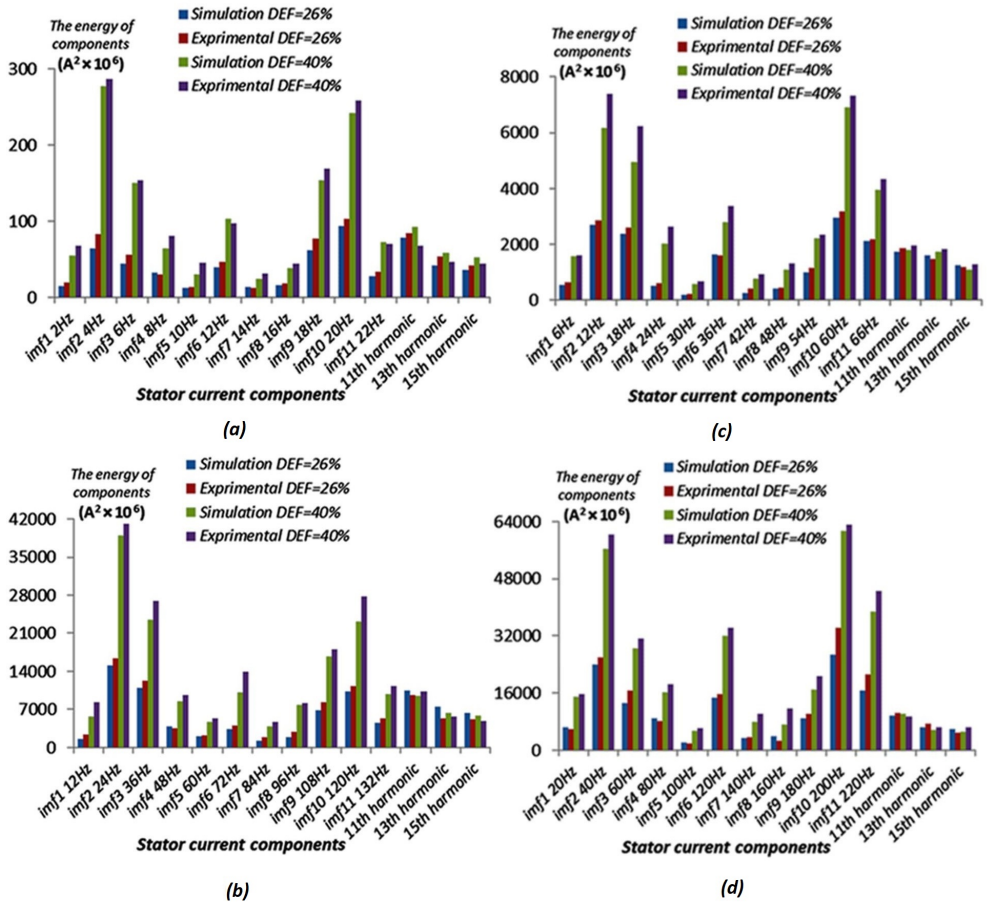

Figure 11. Current components under DE condition with a nonlinear load (a) at 10% of nominal speed, (b) at 30% of nominal speed, (c) at 60% of nominal speed, (d) at nominal speed.

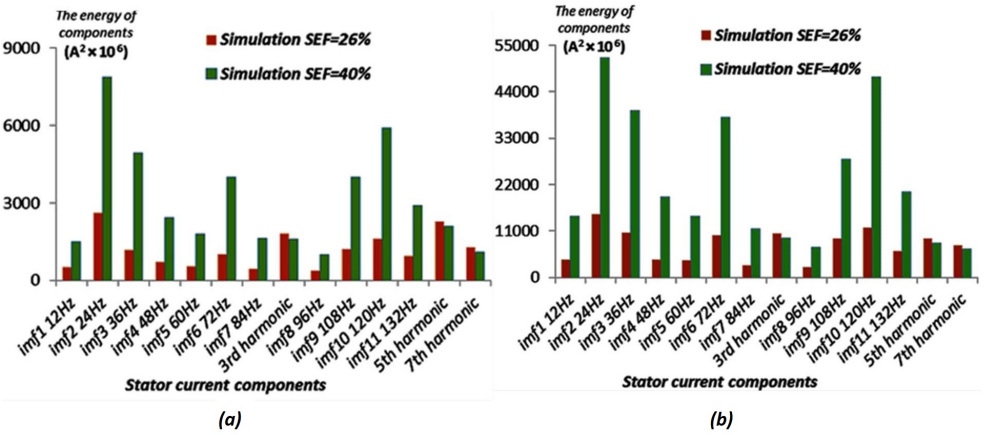

Figure 12. Current components under SE condition with a linear load (a) at 60% of nominal speed, (b) at nominal speed.

List of symbols and abbreviations

AFPM, axial flux permanent magnet; ***IMF***, intrinsic mode functions; ***EMD***, empirical mode decomposition; ***IA***, instantaneous amplitude; ***IF***, instantaneous frequency; ***SE***, static eccentricity; ***DE***, dynamic eccentricity;

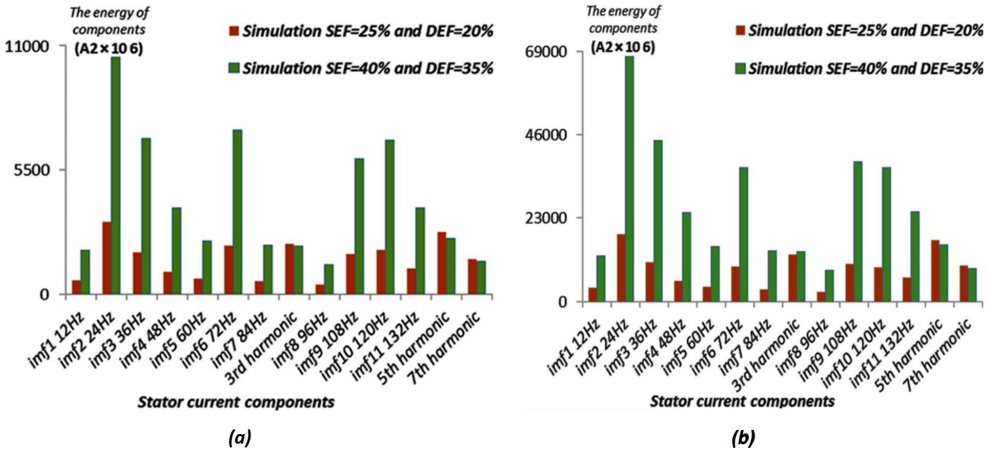

Figure 13. Current components under ME condition with a linear load (a) at 60% of nominal speed, (b) at nominal speed.

ME, mixed eccentricity; ***MCSA***, machine current signature analysis; ***TMCSA***, transient machine current signature analysis; ***FFT***, fast Fourier transform; ***STFT***, short time Fourier transform; ***HHT***, Hilbert-Huang transform; ***EMF***, electromotive force; $\boldsymbol{\beta}$, the angle between rotor and axis of the stator; ***SEF***, static eccentricity factor; ***DEF***, dynamic eccentricity factor; $\boldsymbol{g_0}$, The air gap length in the normal operation of machine; $\boldsymbol{R_{in}}$, the inner radius of the rotor; $\boldsymbol{R_{out}}$, the outer radius of the rotor; $\boldsymbol{\gamma_0}$, The position measuring reference point; $\boldsymbol{\theta}$, the angular position on the stator measured from the reference point; $\boldsymbol{g(\theta, R)}$, the air gap length in all positions of (R, θ); , Permeance of the flux path; ***MMF***, magneto motive force, $\boldsymbol{F(t)}$, magnetic-field motion force; $\boldsymbol{\mu_0}$, the free space permeability of the flux path; $\boldsymbol{\omega}$, the fundamental frequency in rad/s; $\boldsymbol{P}$, the number of pole pairs; $\boldsymbol{B_s}$, the stator air gap field; $\boldsymbol{J_s(\varphi, t)}$, the current density on the stator surface; ***rpm***, round per minute; $\boldsymbol{f_s}$, fundamental frequency; $\boldsymbol{e_{min}[n]}$, local minima points in sampled data; $\boldsymbol{e_{max}[n]}$, local maxima points in sampled data; $*$, points the convolution product; $\boldsymbol{T-F}$, time–frequency.

References

[1] [1] Bruzinga GR, Sguarezi Filho AJ, Pelizari A. Analysis and Design of 3 kW Axial Flux Permanent Magnet Synchronous Motor for Electric Car. IEEE Latin America Transactions 2022; 20 (5): 855–863. doi:10.1109/TLA.2022.9693571

[2] Lai J, Li J, Xiao T. Design of a compact axial flux permanent magnet machine for hybrid electric vehicle. IEEE Transactions on Industrial Electronics 2021; 68 (8): 6630–6639. doi:10.1109/TIE.2020.3008358

[3] Keskin Arabul F, Senol I, Oner Y. Performance analysis of Axial-Flux Induction Motor with Skewed Rotor. Energies 2020; 13 (19), 1–15. doi:10.3390/en13194991

[4] Shao L, Navaratne R, Popescu M, Liu G. Design and Construction of Axial-Flux Permanent Magnet Motors for Electric Propulsion Applications–A Review. IEEE Access 2021; 9: 158998–159017. doi:10.1109/ACCESS.2021.3131000

[5] Wang Q, Zhao F, Yang K. Analysis and optimization of the axial electromagnetic force for an axial-flux permanent magnet Vernier machine. IEEE Transactions on Magnetics 2021; 57 (2): 1–5. doi:10.1109/TMAG.2020.3005216

[6] Gholamian SA, Ardebili M, Abbaszadeh K. Analytic and FEM Evaluation of Power Density for Various Types of Double-Sided Axial Flux Slotted PM Motors. International Journal of Applied Engineering Research 2008; 3 (6): 749–762.

[7] Xia B, Shen JX, Luk PC, Fei W. Comparative study of air cored axial-flux permanent magnet machines with different stator winding configurations. IEEE Transactions on Industry Applications 2015; 62 (2): 846-856. doi:10.1109/TIE.2014.2353012

[8] Nobahari A, Darabi A, Hassannia A. Various skewing arrangements and relative position of dual rotor of an axial flux induction motor, modelling and performance evaluation. IET Electric Power Applications 2018; 12 (4): 575–580. doi:10.1049/iet-epa.2017.0716

[9] Guo B, Du Y, Peng F, Huang Y. Magnetic Field Calculation in Axial Flux Permanent Magnet Motor with Rotor Eccentricity. IEEE Transactions on Magnetics 2022; 58 (9): 1–4. doi:10.1109/TMAG.2022.3185708

[10] Ma C, Gao Y, Degano M, Wang Y, Fang J, Gerada C, Zhou S, Mu Y. Eccentric position diagnosis of static eccentricity fault of external rotor permanent magnet synchronous motor as an in-wheel motor. IET Electric Power Applications 2020; 14 (11): 2263–2272. doi:10.1049/iet-epa.2019.0617

[11] Mirimani SM, Vahedi A, Marignetti F, Di Stefano R. An Online Method for Static Eccentricity Fault Detection in Axial Flux Machines. IEEE Transactions on Industrial Electronics 2015; 62 (3): 1931-1942. doi:10.1109/TIE.2014.2360070

[12] Da Y, Shi X, Krishnamurthy M. A New Approach to Fault Diagnostics for Permanent Magnet Synchronous Machines Using Electromagnetic Signature Analysis. IEEE Transactions on Power Electronics 2013; 28 (8): 4104-4112. doi:10.1109/TPEL.2012.2227808

[13] Park Y, Fernandez D, Lee SB, Hyun D, Jeong M et al. Online Detection of Rotor Eccentricity and Demagnetization Faults in PMSMs Based on Hall-Effect Field Sensor Measurements. IEEE Transactions on Industry Applications 2019; 55 (3): 2499-2509. doi:10.1109/TIA.2018.2886772

[14] Zhang Q, Feng M. Fast Fault Diagnosis Method for Hall Sensors in Brushless DC Motor Drives. IEEE Transactions on Power Electronics 2019; 34 (3): 2585-2596. doi:10.1109/TPEL.2018.2844956

[15] Xia P, Yu Sh, Dou R, Zhai F. Analytical modeling and study on noise characteristics of rotor eccentric SPMSM with unequal magnetic poles structure. Turkish Journal of Electrical Engineering and Computer Sciences 2021; 29(2): 40. doi:10.3906/elk-2006-91

[16] Torregrossa D, Khoobroo A, Fahimi B. Prediction of Acoustic Noise and Torque Pulsation in PM Synchronous Machines with Static Eccentricity and Partial Demagnetization Using Field Reconstruction Method. IEEE Transactions on Industrial Electronics 2012; 59 (2): 934-944. doi:10.1109/TIE.2011.2151810

[17] Chreier L, Bendl J, Chomat M. Analysis of stator and rotor currents and torque of induction machine with rotor-bar faults. Electrical Engineering 2021; 103: 519–528. doi:10.1007/s00202-020-01096-2

[18] Ebrahimi BM, Faiz J. Demagnetization Fault Diagnosis in Surface Mounted Permanent Magnet Synchronous Motors. IEEE Transactions on Magnetics 2013; 49 (3): 1185-1192. doi:10.1109/TMAG.2012.2217978

[19] Ke LV, Gao C, Si J, Feng H, Cao W. Fault coil location of inter-turn short-circuit for direct-drive permanent magnet synchronous motor using knowledge graph. IET Electric Power Applications 2020; 14 (9): 1712–1721. doi:10.1049/iet-epa.2020.0123

[20] Hong J, Hyun D, Kang TJ, Lee SB, Kral CH et al. Detection and Classification of Rotor Demagnetization and Eccentricity Faults for PM Synchronous Motors. IEEE Transactions on Industry Applications 2012; 48 (3): 923-932. doi:10.1109/ECCE.2011.6064103

[21] Akar M, Hekim M, Orhan U. Mechanical fault detection in permanent magnet synchronous motors using equal width discretization-based probability distribution and a neural network model. Turkish Journal of Electrical Engineering and Computer Sciences 2015; 23 (3): 14. doi:10.3906/elk-1210-58

[22] Eker M, Akar M. Eccentricity fault diagnosis in a permanent magnet synchronous motor under non-stationary speed conditions. Turkish Journal of Electrical Engineering and Computer Sciences 2017; 25 (3): 22. doi:10.3906/elk-1601-157

[23] Maouche Y, Oumaamar M, Boucherma M. The Propagation Mechanism of Fault Signatures in Squirrel Cage Induction Motor Drives. Journal of Electrical Engineering & Technology 2019; 14: 121–133. doi:10.1007/s42835-018-00037-1

[24] Rajagopalan S, Aller JM, Restrepo JA, Habetler TG, Harley RG. Detection of Rotor Faults in Brushless DC Motors Operating under Non-stationary Conditions. IEEE Transactions on Industry Applications 2006; 42 (6): 1464-1477. doi:10.1109/TIA.2006.882613

[25] Akar M, Taşkin S, Şeker ŞS, Çankaya İ. Detection of static eccentricity for permanent magnet synchronous motors using the coherence analysis. Turkish Journal of Electrical Engineering and Computer Sciences 2010; 18 (6): 3. doi:10.3906/elk-0911-298

[26] Strangas EG, Aviyente S, Zaidi SSH. Time–Frequency Analysis for Efficient Fault Diagnosis and Failure Prognosis for Interior Permanent-Magnet AC Motors. IEEE Transactions on Industrial Electronics 2008; 55 (12): 4191-4199. doi:10.1109/TIE.2008.2007529

[27] Abubakar U, Mekhilef S, Gaeid KS, Mokhlis H, Almashhadany YI. Induction motor fault detection based on multi-sensory control and wavelet analysis. IET Electric Power Applications 2020; 14 (11): 2051-2061. doi:10.1049/iet-epa.2020.0030

[28] Faiz J, Mazaheri-Tehrani E. Demagnetization Modelling and Fault Diagnosing Techniques in Permanent Magnet Machines under Stationary and Non-stationary Conditions: An Overview. IEEE Transactions on Industry Applications 2017; 53 (3): 2772-2785. doi:10.1109/TIA.2016.2608950

[29] Kaya Y, Kuncan F, Ertunç Metin HM. A new automatic bearing fault size diagnosis using time-frequency images of CWT and deep transfer learning methods. Turkish Journal of Electrical Engineering and Computer Sciences 2022; 30 (5): 12. doi:10.55730/1300-0632.3909

[30] Ramu SK, Irudayaraj GCR, Subramani S, Subramaniam U. Broken rotor bar fault detection using Hilbert transform and neural networks applied to direct torque control of induction motor drive. IET Power Electronics 2020; 13 (15): 3328–3338. doi:10.1049/iet-pel.2019.1543

[31] Elbouchikhi E, Choqueuse V, Amirat Y, Benbouzid MEH, Turri S. An Efficient Hilbert-Huang Transform-Based Bearing Faults Detection in Induction Machines. IEEE Transactions on Energy Conversion 2017; 32 (2): 401-413. doi:10.1109/TEC.2017.2661541

[32] Wang C, Liu X, Chen Z. Incipient Stator Insulation Fault Detection of Permanent Magnet Synchronous Wind Generators Based on Hilbert–Huang Transformation. IEEE Transactions on Magnetics 2014; 50 (1): 1-4. doi:10.1109/TMAG.2014.2318207

[33] Alvarez-Gonzalez F, Griffo A, Wang B. Permanent magnet synchronous machine stator windings fault detection by Hilbert–Huang transform. The Journal of Engineering 2019; 2019 (17): 3505-3509. doi:10.1049/joe.2018.8173

[34] Taran N, Ardebili M. Multi-objective Optimal Design of an Axial Flux Permanent Magnet Generator for Directly Coupled Wind Turbines. International Journal of Scientific and Engineering Research. 2014; 5 (7): 298-305.

[35] Yunkai H, Guo B, Guo Y, Zhu J, Hemeida A et al. Analytical modeling of axial flux PM machines with eccentricities. International Journal of Applied Electromagnetics and Mechanics 2016; 53 (4): 1-21. doi:10.3233/JAE-160106

[36] Rajagopalan S, Roux WL, Habetler TG, Harley RG. Dynamic Eccentricity and Demagnetized Rotor Magnet Detection in Trapezoidal Flux (Brushless DC) Motors Operating Under Different Load Conditions. IEEE Transactions on Power Electronics 2007; 22 (5): 2061-2069. doi:10.1109/TPEL.2007.904183

[37] Ebrahimi BM, Faiz J, Roshtkhari MJ. Static, Dynamic and Mixed Eccentricity Fault Diagnoses in Permanent-Magnet Synchronous Motors. IEEE Transactions on Industrial Electronics 2009; 56 (11): 4727-4739. doi:10.1109/TIE.2009.2029577

[38] Chin R, Kanninen P. The phenomenon of magnetic force: Estimating its effects on wind turbine generators. IEEE Industry Applications Magazine 2013; 19 (4): 39–46. doi:10.1109/MIAS.2012.2215633

[39] Kang CH, Kang KJ, Song JY, Cho YJ, Jang GH. Axial Unbalanced Magnetic Force in a Permanent Magnet Motor Due to a Skewed Magnet and Rotor Eccentricities. IEEE Transactions on Magnetics. 2017; 53 (11): 1–5. doi:10.1109/TMAG.2017.2708319

[40] Huang E. Introduction to the Hilbert-Huang transform and its related mathematical problems. Goddard Institute for Data Analysis: Code, 614.2, NASA/Goddard Space Flight Center, Greenbelt, MD 20771, USA, 2014.

[41] Huang NE, Wu MC, Long SR, Shen SSP, Qu W et al. A confidence limit for the empirical mode decomposition and Hilbert spectral analysis. Proceedings of the Royal Society A. Mathematical, Physical and Engineering Sciences 2003; 459 (2037): 2317-2345. doi:10.1098/rspa.2003.1123

[42] Niu G, Son JD, Widodo A, Yang BS, Hwang DH et al. A comparison of classifier performance for fault diagnosis of induction motor using multi-type signals. Structural Health Monitoring 2007; 6 (3): 215–229. doi:10.1177/1475921707081110

[43] Duda R, Hart PE, Stork DG. Pattern Classification. 2nd ed. New York: Wiley; 2002.